Contents lists available at ScienceDirect

Thin-Walled Structures

journal homepage: www.elsevier.com/locate/tws

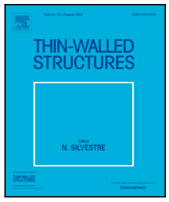

Highlights

Modeling the strain localization of shell elements subjected to combined stretch–bend loads: Application on automotive sheet metal stamping simulations

Thin-Walled Structures xxx (xxxx) xxx

Quoc Tuan Pham*, Md Shafiqul Islam, Alexander Barlo, Mats Sigvant, Lluís Pérez Caro, Kristoffer Trana

- Proposal of the so-called stretching-to-bending ratio, ρ of shell elements
- Proposal of the necking limit curve as a function of ρ
- Calibrate the necking limit curve of two automotive sheet metals: DP800 and AA6016.
- Validate the calibrated AA6016 curve via a test die stamping simulation in AutoForm
- Good agreement with experimental observation on the deformed panel's failure positions.

Graphical abstract and Research highlights will be displayed in online search result lists, the online contents list and the online article, but will not appear in the article PDF file or print unless it is mentioned in the journal specific style requirement. They are displayed in the proof pdf for review purpose only.

Please cite this article as: Q.T. Pham, M.S. Islam, A. Barlo et al., Modeling the strain localization of shell elements subjected to combined stretch–bend loads: Application on automotive sheet metal stamping simulations, Thin-Walled Structures (2023) 110804, https://doi.org/10.1016/j.tws.2023.110804.

TWST: 110804

ARTICLE IN PRESS

Thin-Walled Structures xxx (xxxx) xxx

Contents lists available at ScienceDirect

Thin-Walled Structures

journal homepage: www.elsevier.com/locate/tws

Full length article

Modeling the strain localization of shell elements subjected to combined stretch–bend loads: Application on automotive sheet metal stamping simulations

Quoc Tuan Pham [a,*], Md Shafiqul Islam [a], Alexander Barlo [a], Mats Sigvant [a,b], Lluís Pérez Caro [c], Kristoffer Trana [d]

[a] Department of Mechanical Engineering, Blekinge Institute of Technology, Karlskrona, Sweden
[b] Volvo Cars, Department 81110 Strategy Development, Olofström, Sweden
[c] RISE Research Institutes of Sweden, Component Manufacturing Unit, Olofström, Sweden
[d] Volvo Cars, Department 81151 Product & Process Structures, Olofström, Sweden

ARTICLE INFO

Keywords:
Stretch–bending load
Shell element
Strain localization
Automotive sheet metal
Through-thickness strain gradient

ABSTRACT

This study presents a modeling approach for predicting strain localization during sheet metal stamping processes focused on automotive engineering applications. The so-called stretching-to-bending ratio, ρ, is proposed to characterize the loading conditions acting on an element during stamping processes. Then, localized strain or necking strain is suggested to be a function of ρ. Different stretch–bending tests with different tool radii, i.e., R3, R6, R10, and R50 are conducted for two automotive sheet metals, DP800 and AA6010, to identify their forming limits under combined stretch–bend loads. The calibrated necking limit curve of the AA6016 sheet is then employed in AutoForm R10 software to predict the necking and failure of a stamped panel. Agreement with the experimental observation of failure positions of the panel validates the usefulness of the proposed modeling approach in practice.

1. Introduction

Sheet metal stamping is extensively used in the automotive industry to manufacture medium to large-size parts. In the process, a blank sheet is deformed into the designated shape by using a rigid punch-die system. A deformed part is inferred failure if there exists a strain localization in the form of a localized neck. For decades, failure prediction in stamping processes has been a crucial demand for designing as well as evaluating the formed product.

Since its introduction, the forming limit diagram (FLD) has become an industry standard for evaluating the failure of a formed part. The concept of FLD presents a boundary of forming safety in the principal strain space represented by a forming limit curve (FLC). Although its benefits provided, the use of FLC is limited in several loading conditions, such as non-proportional loads, strain path changes, and combined stretching–bending loads. These loading conditions are more and more common in the current automotive industry to meet the requirements of making complex designed parts and using advanced metallic materials. Various feasible solutions for non-linear load scenarios have been proposed in the literature, for example, stress-based FLD [1], generalized forming limit concept [2], and strain-path independent FLC [3]. The usefulness and efficiency of these solutions have been demonstrated in previous studies. These approaches have been implemented in several commercial software in the field of sheet metal forming analysis, for instance, AutoForm, and PAM-STAMP. However, failure prediction for the blank subjected to a combined bending–stretching load is still challenging.

Looking at previous studies in literature, experiments on stretch–bending of numerous sheet metals pointed out that the necking strain observed in a bending-dominated deformation is higher than that of an in-plane stretching [4–8]. To explore the reasons for the difference, Andersen et al. [9] conducted numerical simulations of the far-field plane-strain tension and plane-strain bending tests for medium-strength steel. They found that the amount of thickness reduction resulted from the strain localization observed in the former case is superior to that of the latter one. Moreover, the failure location of a strip subjected to stretch–bending tests can be classified into three groups with increasing ratio of the bending radius and strip thickness (R/t) [10,11]:

(i) failure at the center of the contact area between the blank and tool curvature,
(ii) failure at the contact border,
(iii) failure outside of the contact region.

Thus, bending deformation contributes significantly to the mechanism of strain localization in sheet metal subjected to stamping processes,

* Corresponding author.
E-mail address: quoc.tuan.pham@bth.se (Q.T. Pham).

https://doi.org/10.1016/j.tws.2023.110804
Received 2 February 2023; Received in revised form 15 April 2023; Accepted 19 April 2023
Available online xxxx
0263-8231/© 2023 The Author(s). Published by Elsevier Ltd. This is an open access article under the CC BY license (http://creativecommons.org/licenses/by/4.0/).

where combinations of stretching and bending loads have frequently occurred.

On the one hand, efforts have been made to analytically predict the failure of combined stretch–bending processes. Xia and Zeng [12] presented a theoretical formulation for bending-enhanced FLC that makes use of the R/t ratio in the plasticity equations. Lee and Barlat [13] developed an analytical model to evaluate the failure of stretch–bending tests, which is based on several process parameters (the tool radius, sheet thickness, wrap angle with friction) and the tensile properties of the tested materials.

On the other hand, different approaches have been proposed to construct the forming limits that couple the effects of stretching and bending deformation. Tharrett and Stoughton [14] proposed the well-known "concave-side rule" (CSR) based on the observation of strain gradient through the thickness of the deformed sheets. This model suggests that the localized neck occurs at the convex surface as soon as the strain on the concave side reaches the forming limit under in-plane stretching. Later, this model was re-defined considering the stress gradient [15]. Apart from these methods, Morales-Palma et al. [16] proposed a two-step deformation procedure that ideally decomposes the deformation observed during a stretch–bending procedure into pure bending and pure stretching deformation sequentially. They adopted the critical distance method [17] to provide more flexible descriptions of failure by necking of ductile fracture. Alternatively, Sriram et al. [18] proposed the stretch bendability index (SBI) concept, which is defined as the ratio between the limit strain under a pure stretching load and those of the considering stretch–bending process, to determine the limits of bending under tension loads. They suggested using the SBI as a function of the R/t ratio to determine the forming limits of several structural and skin steels. Wu et al. [19] accumulated a bending modification to the bending under tension limits. In another way, Neuhauser et al. [20] introduced an additional amount of bending dependency to the traditional FLC, which was formulated as a power law of the superimposed bending component t/R.

The summarized works clarify the importance of accurately incorporating the bending effect in evaluating the failure of stamped parts. For this purpose, numerical simulation with the finite element (FE) method has been demonstrated as an efficient tool. However, the use of the aforementioned methods in the numerical simulation of stamping processes is conservative and inadequate, especially in the case that the tools have multiple radii or complex shapes. Furthermore, the use of shell elements, which are mainly used in stamping simulations due to the time efficiency, in predicting failure appears with several challenges. Practices indicate the size-dependent response of shell elements [21], where a finer mesh size seems to increase the predicted necking strain of stamped parts. Furthermore, shell elements cannot provide sufficient predictions of material behavior beyond and after the neck initiation, although their predictability for the pre-necking behavior has been confirmed [22,23]. The reason for the insufficient is due to the highly inhomogeneous strain distribution inside and outside the neck, which results in the out-of-plane deformation and though-thickness stress components. Therefore, a very fine mesh is mandated for reproducing sheet metal necking and failure in numerical simulations, e.g., element sizes of 0.1 mm and smaller have been adopted in the cited works [24–26]. However, such a small mesh size is impractical to use in industrial applications due to the high computational time and cost.

Several approaches have been proposed to cope with these issues. Neukamm et al. [27,28] developed a generalized incremental stress state-dependent damage model (GISSMO) to fully describe the ductile damage, including material softening and fracture. In this model, the damage is examined by an indicator of which value is accumulated as deformation progresses. Later, the model was extended to consider the effect of Lode angle [29] as well as stress triaxiality [30]. Borrvall et al. [31] introduced a damage initiation and evolution model (DIEM), which uses a necking indicator to manage the damage-induced softening behavior. Pack and Mohr [23] presented the domain of shell to solid equivalence (DSSE), which is a transformation of the theoretical FLC based on the MK method [32]. Woelke [33] implemented a modified Gurson's damage model [34] in numerical simulation with shell elements. Alternatively, Stoughton and Yoon [15] suggested using the stress-based FLD combined with the maximum shear criterion to capture the failure in simulations. In particular, the bending effect is overlooked in these methods.

This study presents a modeling approach to capture the bending effect on strain localization observed in stamping simulations with shell elements. A stretching-to-bending ratio ρ is proposed to characterize the deformation resulting in the combined stretch–bending loads. Hence, the limit strain observed on the specimen's surface is suggested to be a function of ρ. Therefore, a hybrid numerical–experimental method is adopted to construct the necking limit curve for DP800 and AA6016 sheets by using the results of four lab-scale stretch–bend tests. The derived necking limit curve of AA6016 is then employed in AutoForm R10 to simulate a production-like stamping test. The predicted strain localization is compared with experimental observation to validate the usefulness of the proposed approach.

2. Strain localization under stretch–bend deformation

2.1. Stretching-to-bending ratio

Previous studies demonstrate the variation in the failure position of strips subjected to stretch–bending tests with different tool radii [10,11]. Besides the bending radius, other process parameters, for instance, the friction condition and the forming speed, have been confirmed their effects on the level of necking strains [35,36]. Therefore, using only the tool radius for accounting for the bending effect on a stamped sheet's strain localization seems insufficient. Moreover, the contribution of stretching and bending to the material's response under complex loads is indistinguishable. It is a demand to quantify these effects on the material's deformation simultaneously.

Chung et al. [37] suggested that strain localization is an intrinsic property of sheet metals. Motivated by this comment, it is suggested that the deformation characteristics, such as the stress state or strain state, should be used to identify the necking status of an element. The strain state may prefer because the strain components are measurable. Therefore, this study suggests characterizing the status of strain localization of a considering element via its strain gradient through the thickness direction. For this purpose, the so-called stretching-to-bending ratio ρ, is formulated as follows:

$$\rho = \frac{1}{2}\frac{|\varepsilon_1^u - \varepsilon_1^l|}{\max(|\varepsilon_1^u|, |\varepsilon_1^l|)} \tag{1}$$

where superscripts "u" and "l" denote the upper and lower layers of the element, ε_1 denotes the major strain of the element. Under pure stretching, the strain values estimated for the upper and lower layers are equal and $\rho = 0$. In contrast, $\rho = 1$ indicates a pure bending load where the strain values of the upper and lower layers are opposite. A particular value of ρ represents a degree of stretch–bend combination status of the element.

The formulation expressed in Eq. (1) is similar to the one introduced in [38], except that the plastic strain components were used in the cited work. However, this variable is used in a different way here. In the work of Costas et al. [38], ρ was used as a scaling factor to combine the effects of bending and stretching deformations in the Cockcroft–Latham fracture criterion [39], whereas this variable is used to classify the loading condition acting on the element in this study.

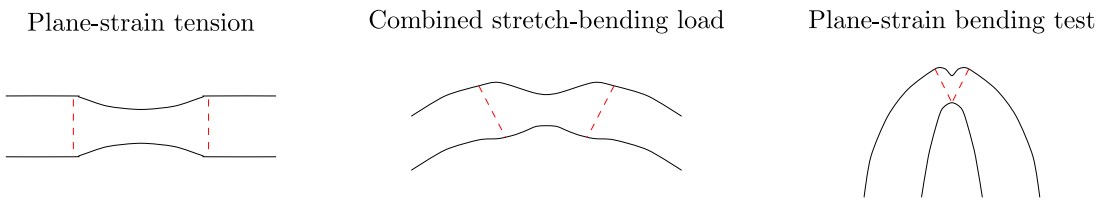

Fig. 1. Illustration of sheet metal's necking region (bounded by dashed lines) in different load cases.

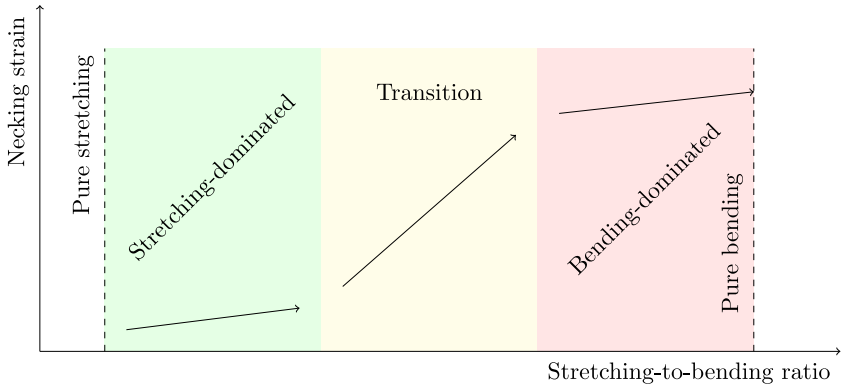

Fig. 2. Concept of the proposed stretch–bend forming limit.

2.2. Necking limit under stretch–bending loads

As discussed before, failure in laborious stretch–bending tests can be classified into three groups according to the failure position. These failure groups are suggested to be related to three loading conditions: stretching-dominated, bending-dominated, and transition. Fig. 1 illustrates the conceptualized through-thickness deformation observed in these loading conditions. Under a pure stretching load such as a plane-strain tension test, the neck is initiated and formulated equally in both surfaces of the deformed specimen. Consequently, the out-of-plane deformation is only taken place inside the neck and $\rho = 0$ in the entire specimen. In contrast, under a bending-dominated deformation such as a plane-strain bending test (i.e., ISO 7438-2016, E [40]), the neck is apparently observed on the top (convex) surface; meanwhile, another neck on the bottom (concave) surface is negligible. In such a case, the strain generated on the concave surface is close to zero (see [41,9,42]) leading to $\rho \approx 0.5$. Although the out-of-plane deformation may occur in the whole specimen, the deformation of the necking region is more complex due to the appearance of the thickness reduction. Moreover, during a stamping process in which the tool radius ranges from 1 mm to 50 mm conventionally, material deformation is somewhat in between the two mentioned test cases, where the neck can be observed in both convex and concave surfaces. Consequently, the ρ value of an element inside the neck varies from 0 to 0.5 according to the loading conditions acting on the element. Although there is no direct link between the ρ value and the out-of-plane deformation, this parameter can be used to identify the degree of combination of the stretching and bending loads acting on the element and clarify how complicated the out-of-plane deformation is generated. Thus, a critical strain can be constructed based on this parameter, which acts as a reference for the critical deformation or the necking stage of the considering element.

Based on the discussion, Fig. 2 presents the concept of the stretching-to-bending ratio. Under the stretching-dominated deformation, it is suggested that the necking strain increases gradually from the limit of pure stretching deformation within a slight slope as ρ increases. In the transition region from the stretching-dominated to the bending-dominated regions, the slope of increase is much steeper. However, the value of necking strain saturates to the upper limit of pure bending condition. Thus, the necking strain of bending-involved deformation is increased as the stretching-to-bending ratio increases.

In this study, the necking initiation is suggested to occur as soon as the major strain exceeds a critical value determined by the Boltzmann function below:

$$\varepsilon_1^* = A_2 + \frac{A_1 - A_2}{1 + exp\left(\frac{\rho - \rho_0}{S}\right)}. \quad (2)$$

In this equation, A_1 is the lower limit of the pure stretching deformation, A_2 is the upper limit of the pure bending deformation, ρ_0 is the coefficient of the transition from stretching-dominated to bending-dominated deformation, S is the scaling factor used to fit the function to the experimental data.

It is worth noticing that various local extremes of deformation can be formulated within a simulated part. The deformation of elements modeled in these extreme regions is monitored under different stretching-to-bending ratios due to their generated strain gradients. Therefore, the possibility of necking occurrence is a competition between these elements relied on their stretching-to-bending ratios and strains induced. Furthermore, the model adopts the traditional FLC as the lower limits of the pure stretching deformation. That allows determining the necking strain of elements subjected to other forming modes, for example, uniaxial tension or biaxial tension.

3. Experimental procedure

The tested materials in this study are DP800 and AA6016 sheets, which were supported by Volvo Cars (VCBC). The thickness of both materials is 1.2 mm. An experimental campaign is carried out to characterize material properties as well as to examine the strain localization under complex stretch–bending loads.

3.1. Material characterization tests

Uniaxial tensile tests are conducted for the investigated materials following the ISO 6892-1:2009 standard. Specimens are prepared in three orientations, including the rolling direction (RD), diagonal direction (DD), and transversal direction (TD). The tests are conducted under a strain rate of 0.0014 s^{-1} up to the 0.2% engineering strain followed by a strain rate of 0.004 s^{-1} up to fracture. The testing period with a lower strain rate aims to provide reliable data for determining the

Table 1
Material properties obtained from uniaxial tests of the tested materials.

Material	DP800			AA6016		
Orientation	RD	DD	TD	RD	DD	TD
Young modulus (GPa)	186	193	204	68	67	66
Yield stress (MPa)	506.7	498.1	509.5	118.5	113.5	112.4
Ultimate tensile strength (MPa)	853.2	847.2	864.7	296.8	295.7	293.9
Maximum uniform deformation (%)	11.96	12.66	13.96	21.55	23.88	23.14
Elongation at fracture (%)	22.06	19.17	21.27	23.71	26.64	25.70
Lankford coefficient	0.678	0.875	0.844	0.735	0.542	0.680

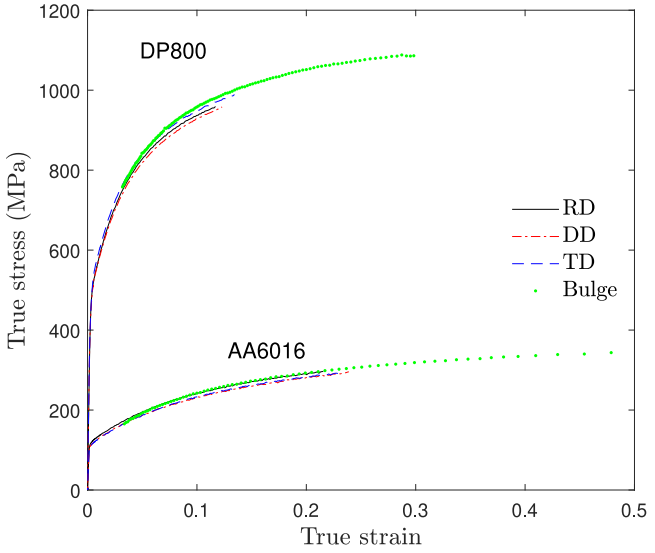

Fig. 3. Comparison of stress–strain curves obtained from uniaxial and bulge tests of the tested materials.

material's properties in elastic deformation. During the tests, ARAMIS™ digital image correlation (DIC) system is used to monitor the entire strain field. Whereas a load cell mounted on the upper cross-head is used to acquire the axial forces. Table 1 reports the material properties obtained from the uniaxial tensile tests.

In addition, a viscous bulge test is performed at a constant punch speed of 5 mm/s to examine the stress–strain relationship in a larger strain range, i.e., in the post-necking ranges. The importance of the post-necking hardening behavior in predicting strain localization of sheet metals has been demonstrated in the previous study [43]. In addition, the test induces material behavior under the balanced-biaxial tension. The ARAMIS™ system is used to capture the strain evolution during the test. More detail on the testing condition can be found in Sigvant et al. [44] and is not repeated here.

Fig. 3 shows true stress–strain curves obtained from uniaxial tensile tests compared to the data derived from the bulge test for both materials. As seen in this figure, the bulge stresses are always higher than that of the uniaxial tensile tests. The comparison demonstrates the anisotropy of the investigated materials.

3.2. Stretch–bend tests

A stretch–bending setup was specially developed at VCBC to characterize material deformation under combined stretching and bending loads. Fig. 4a shows a sectional view of the stretch–bend test observed in the simulation software AutoForm R10. Additionally, Fig. 4b illustrates one of the punches used in the tests. In this setup, the punch is shifted 6 mm to the right of the center of the specimen aiming to eliminate the stochastic failure position. In this study, three-punch radii of 3, 6, and 10 mm are used to generate different loading scenarios, whereas the bigger curvature on the punch is used to centralize the failure position on the deformed specimen. A rectangular blank of 200 × 90 mm is used in each test. It is noted that the longitudinal direction of the blank is along the rolling direction of the sheet. In addition, a blank holder force of 100 kN is applied to clamp the blank sheet with a draw bead.

In addition, a Nakajima test is conducted to examine the strain localization on the specimen under the plane strain tension following the ISO 12004-2 standard. Within this test, a hemispherical punch of 100 mm diameter is used to deform a blank of 125 mm width under a constant forming speed of 25 mm/s. A blank holder force of 300 kN is applied to prevent the draw-in of the blank. Before testing, lubrication of mild-oil is applied to reduce the friction between the blank and punch.

During these tests, the ARAMIS™ system is used to monitor the strain evolution on the outer surface of the tested specimens. Fig. 5 shows the deformed DP800 specimens obtained from these stretch–bending tests. As seen in this figure, the failure positions in the contact areas varied according to different punch radii. In the case of the R3 punch, the crack was observed at nearly the center of the punch, while the crack is outside of the contact region of the R10 punch. The observation demonstrates the different loading scenarios generated in these tests.

4. Finite element simulation

4.1. Constitutive equations

In a finite element (FE) simulation, material behavior is modeled by constitutive equations. This section details the equations used for simulating different forming processes of the investigated materials.

For this purpose, a power law proposed by Swift [45] is adopted to describe the hardening behavior of DP800; meanwhile, the Hockett–Sherby model [46] is applied to the AA6016 sheet. The formulations of these hardening laws are expressed as follows:

$$\text{Swift: } H(\bar{\varepsilon}) = c_1(c_2 + \bar{\varepsilon})^{c_3} \tag{3}$$

$$\text{Hockett-Sherby: } H(\bar{\varepsilon}) = c_1 - c_2 exp(-c_3(\bar{\varepsilon}^{c_4})) \tag{4}$$

where $c_1 \sim c_4$ are material parameters.

In addition, a yield function is required to govern the material's response under multi-axial stress states. According to the material's anisotropy reported in Table 1, the BBC05 function presented in [47] is adopted to describe the yield surface. Since the associated flow rule is adopted, both yield and potential surfaces are described by the same function, of which the equivalent stress is given as follows:

$$\text{BBC05: } \bar{\sigma} = \left[a|\Lambda + \Gamma|^m + a|\Lambda - \Gamma|^m + b|\Lambda + \Psi|^m + b|\Lambda - \Psi|^m\right]^{1/m} \tag{5}$$

where a, b, and m are material's parameters; Λ, Γ, and Ψ are functions of stress tensor components, which can be expressed as follows:

$$\begin{aligned} \Lambda &= L\sigma_{11} + M\sigma_{22} \\ \Gamma &= \sqrt{(N\sigma_{11} - P\sigma_{22})^2 + \sigma_{12}\sigma_{21}} \\ \Psi &= \sqrt{(Q\sigma_{11} - R\sigma_{22})^2 + \sigma_{12}\sigma_{21}} \end{aligned} \tag{6}$$

where L, M, N, P, Q, and R are material's parameters.

4.2. Parameter calibration

Parameters of hardening laws are identified by the curve-fitting method and reported in Table 2. Fig. 6 depicts the identified hardening laws compared to the experimental data to demonstrate their accuracy.

To identify the parameters of the yield function for each investigated material, the flow stresses reported in Fig. 3 are normalized to the stress–strain data obtained from the UT of the RD specimen. In addition, the Lankford coefficients determined from UT tests are calculated using

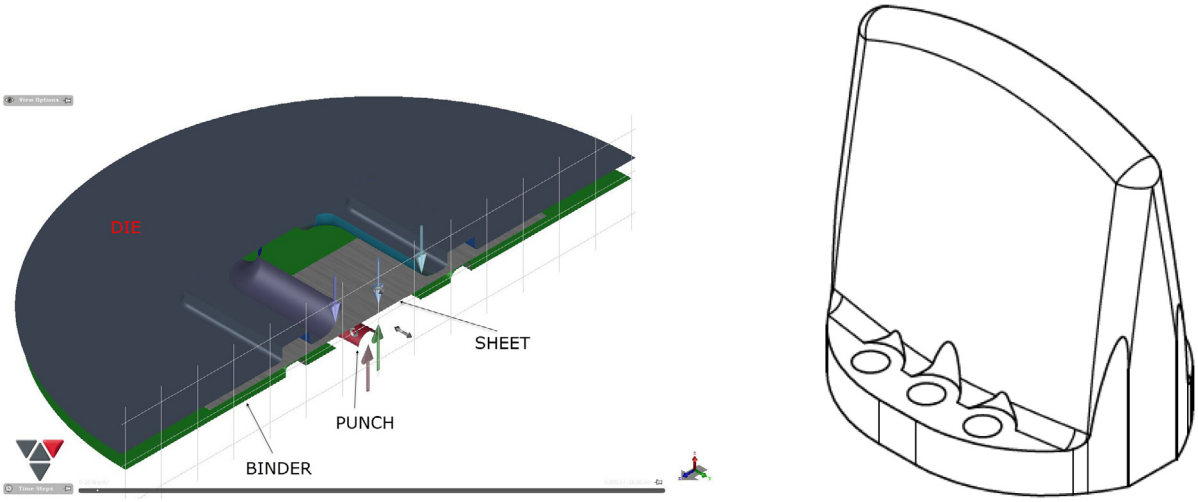

(a) A section view of the stretch-bend test (b) An illustration of the R6 punch

Fig. 4. Detail of the stretch–bending test.

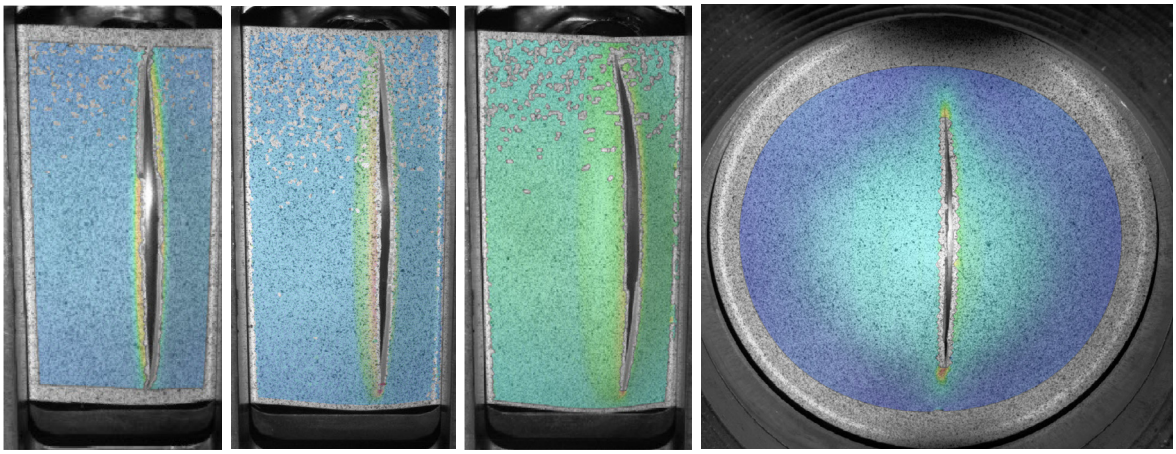

(a) R3 (b) R6 (c) R10 (d) R50-Nakajima test

Fig. 5. Fracture in DP800 specimens obtained from the stretch–bend tests.

Table 2
Material parameters imposed in autoform software for simulations.

Hardening law	Swift			Hockett-Sherby					
	c_1	c_2	c_3	c_1	c_2	c_3	c_4		
DP800	1363.43	0.00014	0.165	–	–	–	–		
AA6016	–	–	–	364.3	255.0	4.52	0.784		
Yield function	BBC05								
	σ_0	σ_{45}	σ_{90}	σ_b	r_0	r_{45}	r_{90}	r_b	m
DP800	1	0.9945	1.0126	0.9935	0.678	0.875	0.844	1.023	6.2
AA6016	1	0.9709	9777	0.9983	0.735	0.542	0.68	1.007	8

the built-in function in the ARAMIS software. In addition, the biaxial coefficient $r_b = \dot{\varepsilon_{yy}}/\dot{\varepsilon_{xx}}$, which characterizes the normal vector of the yield surface under the equi-biaxial stress state, is identified using the bulge test's data. Table 2 reports the identified input parameters (i.e., σ_0, σ_{45}, σ_{90}, σ_b, r_0, r_{45}, r_{90}, and r_b) for calibrating the yield function of the tested materials. Furthermore, these parameters are directly put into the simulation software AutoForm R10 to conduct numerical analysis. For the sake of completeness, Fig. 7 presents the yield locus of the calibrated yield function of the tested materials.

4.3. FEM simulation

Numerical simulations of the combined stretch–bending tests are conducted by using AutoForm R10 software. These models are executed with a constant ram velocity of 25 mm/s since no rate-dependent material model is imposed. In each simulation, the blank is meshed using the triangular Elasto-Plastic Shell elements (EPS-11) with 11 integration points through the thickness. This element type is commonly recommended to simulate the stamping procedure [48]. The initial element size is set at 1 mm with a mesh tolerance of 0.01 mm. In addition, the mesh adaptive level 2 is adopted in the regions where the small tool curvatures come into contact with the blank. Mohr–Coulomb friction coefficients are assigned to different contact pairs between blank and tools. These friction coefficients were calibrated in the previous study [49] and are not repeated here.

Figs. 8–11 show comparisons between the measured and predicted results observed in each test. In detail, Figs. 8a and 8c compare the measured and predicted force–displacement curves of the stretch–bending test with a punch radius of 3 mm (R3) for two tested materials, respectively. In addition, the strain evolution of a critical element located at the center of the necking region (see Figs. 8b and 8d) is compared to the corresponding predictions of AutoForm. These comparisons validate the accuracy of the developed numerical model,

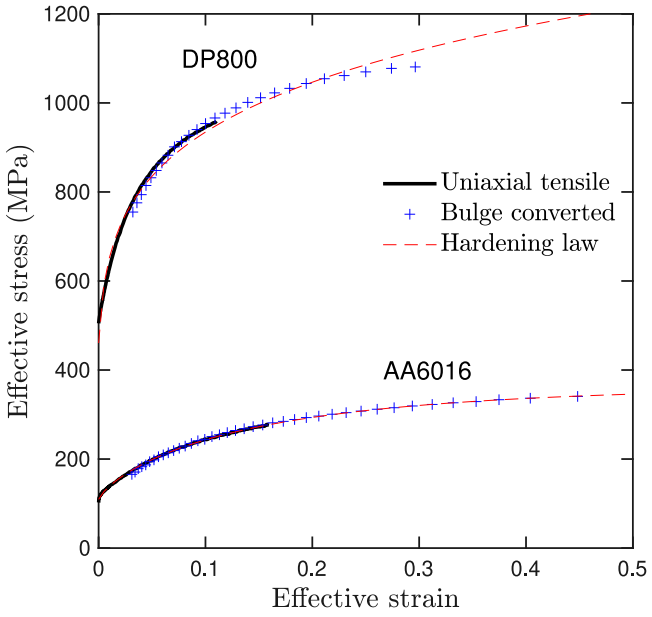

Fig. 6. Effective stress–strain curves obtained from uniaxial tensile and bulge tests of DP800 and AA6016 sheets.

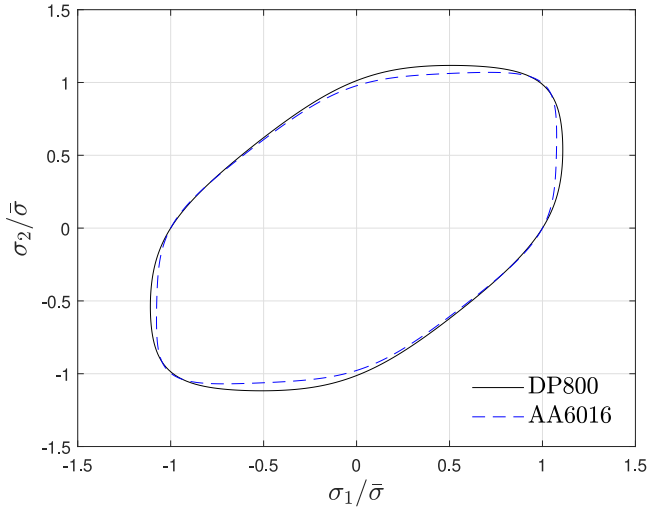

Fig. 7. Yield loci of the calibrated yield functions.

which provided excellent predictions for both punch's force–stroke curves and strain histories. Furthermore, the necking detection method proposed by Sigvant et al. [50] is adopted to determine the initiation of the localized neck. In these tests, the strain localization is supposed to occur at a stroke of 12.1 mm for DP800 and 15.0 mm for AA6016 sheets. Therefore, Figs. 8b and 8d show the major strain distribution on the outer surface of the deformed specimens captured at the necking stage. The comparison of the strain distribution confirms the reliability of the numerical simulation to describe the plastic deformation of the tested coupons.

Similarly, comparison results made for other stretch–bending tests (R6, R10 stretch–bend, and Nakajima tests) are reported in Figs. 9–11 (see Appendix for the comparison of the strain distribution on the deformed specimens). These comparisons demonstrate that the developed numerical simulations sufficiently describe the material responses observed in different stretch–bending scenarios. Furthermore, the DIC-measured data are used to determine the stage at which the strain localization has occurred in each test. Accordingly, the maximum strain

Table 3
Characterization of the tested materials at the necking stage of the stretch–bending tests.

Material	DP800				AA6016			
Tool radius	R3	R6	R10	R50	R3	R6	R10	R50
Punch stroke (mm)	12.1	14.48	15.86	22.6	13.7	14.93	16.15	29.5
Measured necking strain	0.339	0.268	0.206	0.150	0.284	0.234	0.209	0.191
Stretching-to-bending (ρ)	0.321	0.279	0.226	0.076	0.404	0.296	0.207	0.058

Table 4
Calibrated parameters of the proposed stretch–bending forming limit of the tested materials.

Parameter	A_1	A_2	ρ_0	S
DP800	0.144	0.653	0.351	0.063
AA6016	0.185	0.407	0.426	0.104

value observed at this stage is adopted as the measured necking strain of the corresponding test case.

Based on simulated results, Fig. 12 shows the evolution of the stretching-to-bending ratio ρ, which was quantified for the critical element of each test, according to the punch stroke. As seen in this figure, the stretching-to-bending ratio always reaches its maximum at an early stage of deformation, i.e., when the punch dents into the blank. However, the ratio decreased afterward as the deformation continued. In all tests, the strain localization is recorded at extensive deformations with high punch strokes. Additionally, increasing the tool radius decreases the stretching-to-bending ratio observed at the necking condition for both tested materials. Moreover, the variation range of the derived stretching-to-bending values of AA6016 is larger than the DP800 sheet.

Table 3 summarizes the stretching-to-bending ratios determined at the necking stage of these tests and the corresponding measured necking strains for the investigated materials. As seen in this table, the difference in these necking strains is abundant, even though all these tests mainly produce plane-strain deformation on the specimen. The variation of the necking strains verifies the significance of the bending effect on the material's formability when they are subjected to stamping.

4.4. Construction of the necking limits

Based on the stretching-to-bending ratios and necking strains identified in the previous subsection, the necking limits under stretch–bend combined loads are constructed by fitting Eq. (2) with the experimental data. Table 4 reports the identified parameters of the necking limit curves of the tested materials. Moreover, Fig. 13 shows the identified necking limit curve of the tested materials. In addition, the reference fracture strains of similar materials to the tested one identified in cited works [51,41,52] are reported in this figure for comparisons. In detail, Kim and Hance [51] performed a series of VDA 238-100 plate bending tests [53] on four different advanced high-strength sheets of steel in class 780, which contain different thicknesses ranging from 1.4 mm to 1.6 mm. Their results indicate that the fracture strains of the bending tests range from 0.55 to 0.65 based on different tested materials. Using the VDA 238-100 tests, the fracture strains of AA6016 sheets with a range of thickness from 1 mm to 2 mm were identified in the range from 0.7 to 1.1 roundly [41,52].

As seen in Fig. 13, the predicted forming limits are comparable to the reference fracture strains. For DP800 material, the expected necking limits in the bending-dominated regime (i.e., $\rho > 0.5$) are closed up to the reference fracture strains. In contrast, the forming limits of the AA6016 sheet are much lower than the reference fracture strains. The comparison concurs with the results reported in the literature, where the difference between the necking strain and fracture strain of the AA6016 sheet is larger than that of the DP800 sheet.

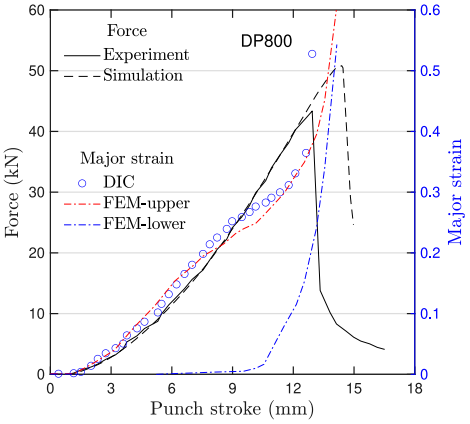

(a) DP800: punch force-stroke curve and strain evolution of a critical element

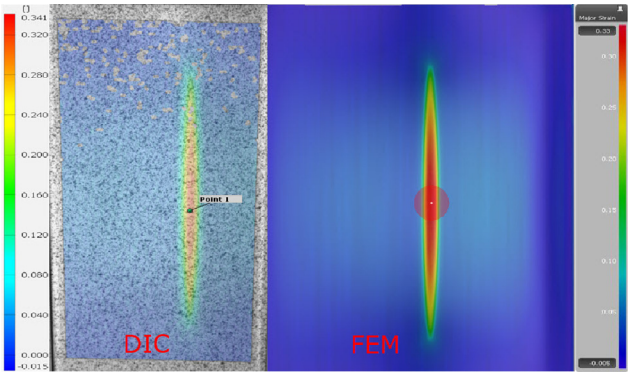

(b) DP800: strain distribution on the outer surface of the deformed specimen at the stage of strain localization

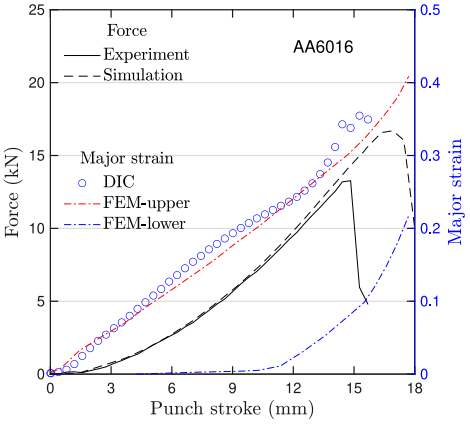

(c) AA6016: punch force-stroke curve and strain evolution of a critical element

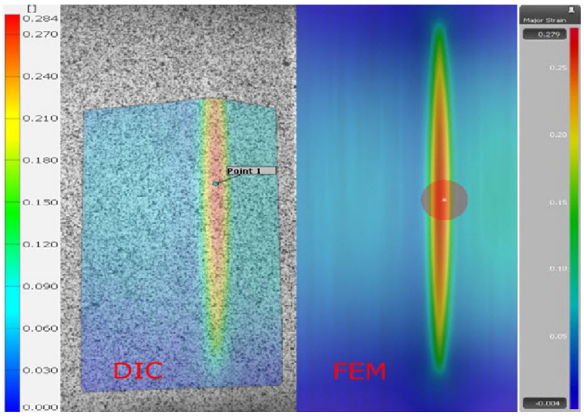

(d) AA6016: strain distribution on the outer surface of the deformed specimen at the stage of strain localization

Fig. 8. Comparison between the measured and simulated results of the R3 stretch–bend test.

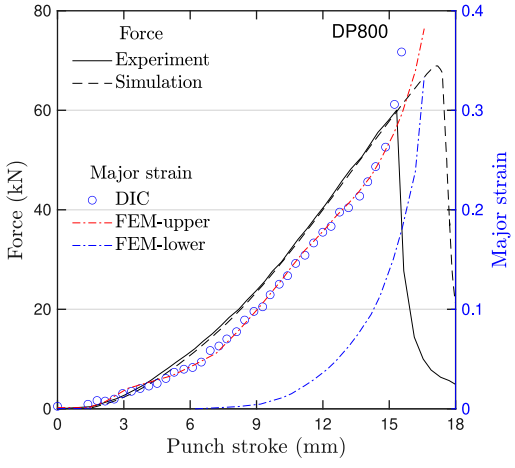

(a) Punch force-stroke curve and strain evolution of a critical element of DP800

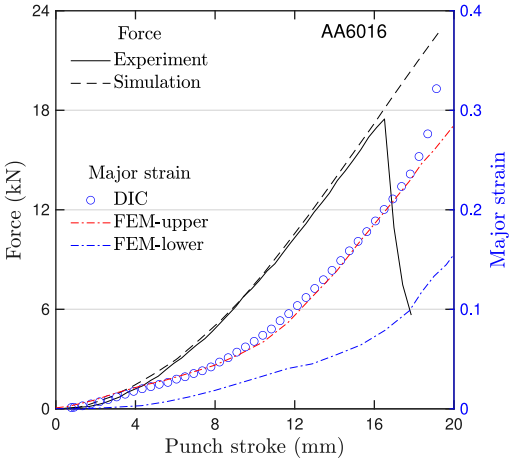

(b) Punch force-stroke curve and strain evolution of a critical element of AA6016

Fig. 9. Comparison between the measured and simulated results of the R6 stretch–bend test.

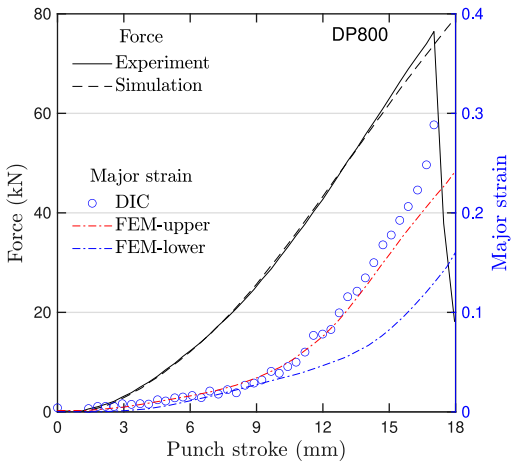

(a) Punch force-stroke curve and strain evolution of a critical element of DP800

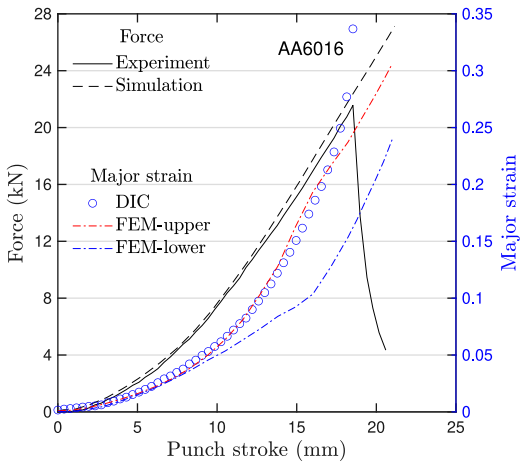

(b) Punch force-stroke curve and strain evolution of a critical element of AA6016

Fig. 10. Comparison between the measured and simulated results of the R10 stretch–bend test.

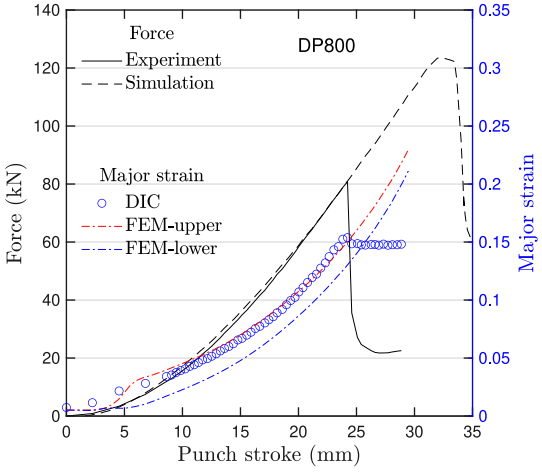

(a) Punch force-stroke curve and strain evolution of a critical element of DP800

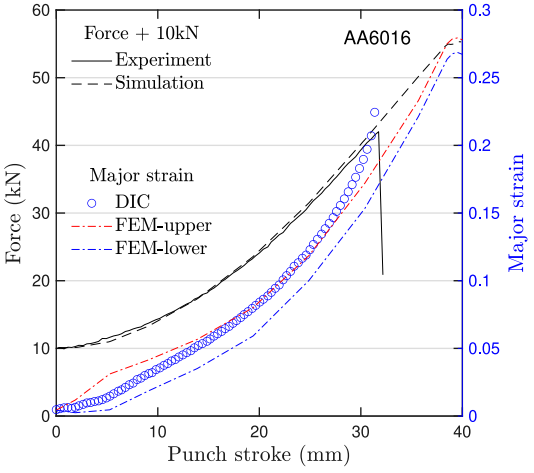

(b) Punch force-stroke curve and strain evolution of a critical element of AA6016

Fig. 11. Comparison between the measured and simulated results of the R50 Nakajima test.

In order to use the constructed necking limits in practice, the following necking index is defined:

$$\text{Necking index: } \xi = \frac{\max(|\varepsilon_1^u|, |\varepsilon_1^l|)}{\varepsilon_1^*(\rho)} > c_0. \tag{7}$$

where c_0 is a constant indicating the necking condition. In the ideal condition, the value of c_0 should be one. However, the simulated strain evolution may not always be coincided with the measurement perfectly, especially in the necking stages. Therefore, the parameter c_0 is used to adapt the simulation to the measurement.

Table 5 reports the calculated necking indexes in the simulations of the stretch–bending tests of two tested materials. As seen in this table, the necking index decreases as the tool radius increases, except for the case of the R6 test for AA6016. It is remarkable that the order of the necking indexes co-occurs with the locality (i.e., the quantity of local deformation) of these tests, see Appendix. The results reveal the difficulty in predicting strain localization in the simulation of large-size parts.

Table 5
Necking index calculated at the necking stage of the stretch–bend tests.

Material	DP800				AA6016			
Tool radius	R3	R6	R10	R50	R3	R6	R10	R50
Predicted necking strain	0.327	0.245	0.183	0.130	0.279	0.2	0.196	0.163
Necking index (ξ)	0.965	0.914	0.889	0.865	0.982	0.854	0.938	0.853

5. Validation

5.1. VCBC test die

A stamping test die was developed at VCBC to characterize the bending effect on the necking and fracture of automotive sheet metals. The test die comprises four rows of sub-punches with adjustable shims to vary the punch strokes. Fig. 14 presents an AA6016 panel stamped with the test die. The sub-punches were made with two radii, 4 mm and 8 mm. Numbers in the figure indicate the shim height amount of the corresponding sub-punch, while the colors indicate the quality of

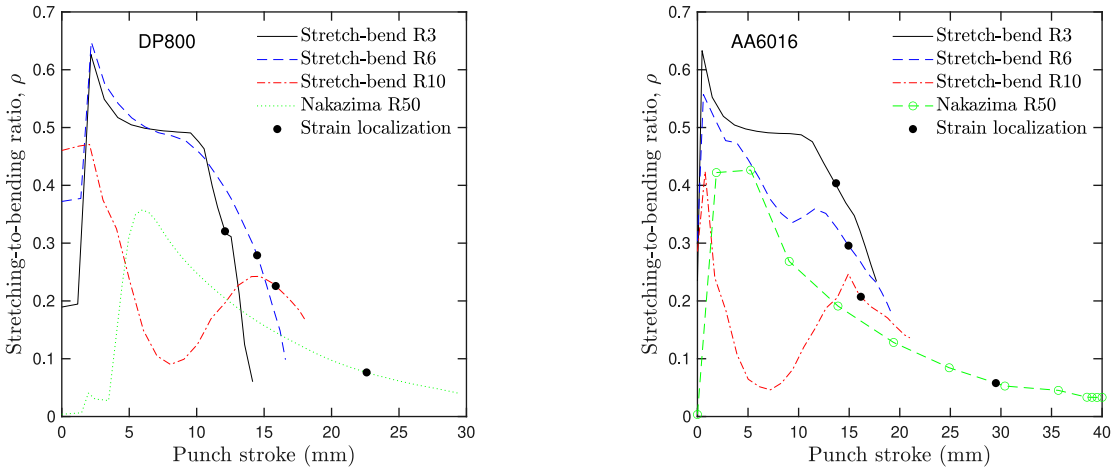

(a) DP800 (b) AA6016

Fig. 12. Evolution of the stretching-to-bending ratio of critical elements observed in the stretch–bend tests.

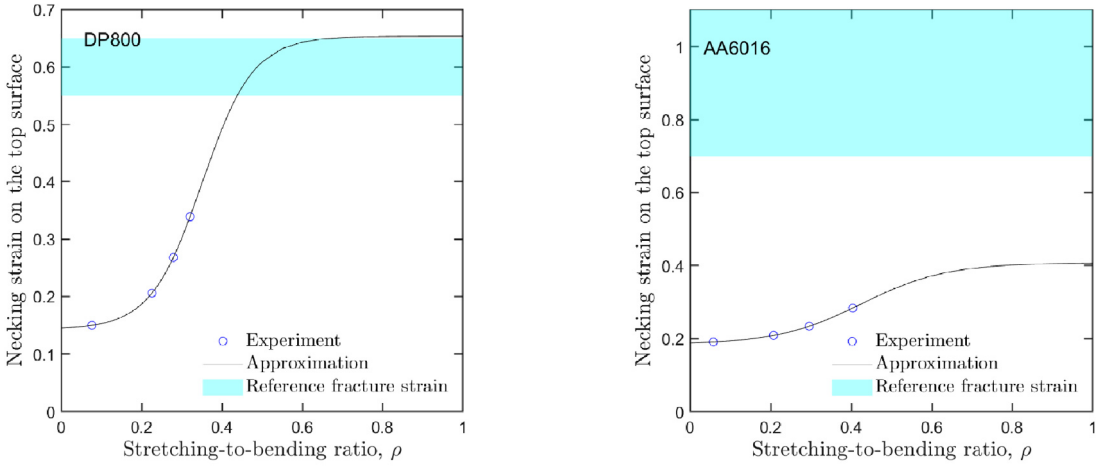

(a) DP800 (b) AA6016

Fig. 13. Forming limit of the tested materials under combined stretch–bend loads.

the deformed sheet in the corresponding region. The surface quality is classified into "OK", "surface necking", "necking", and "crack" status, according to the VCBC standard. Fig. 15 shows an example of the evaluation results of an aluminum panel conducted at VCBC, which indicates the conditions of surface necking, necking, and crack.

For comparison purposes, each stamped region was given a concatenated name. For instance, the "A1" indicates the top-left region, and the "D4" indicates the bottom-right region, as shown in Fig. 14. Based on the evaluation of VCBC, the crack was observed at four regions (i.e., A4, B6, C6, and D4), whereas the necking was observed at six other regions. Others were safe, except for A2 and B4 at which the surface necking appeared. Almost failures were observed at the panel's top surface, excluding the failure of C5 and C6 happened at the bottom surface.

Simulation of the VCBC test die is selected to validate the usefulness of the established stretch–bend necking limits due to several benefits:

(i) The test depicts a more production-like setup than the lab-scale testing methods because the dimension of the initial blank is 1790 × 1110 mm;
(ii) The test die deforms the blank with various bending radii varied in a wide range of tool curvatures from 4 mm to 8 mm;
(iii) Complex loading conditions such as bending, bending–reverse-bending, and combined stretch–bending are generated on different regions of the sheet.

5.2. Simulation of the VCBC test die

A finite element model is developed in AutoForm R10 software to simulate the stamping procedure of the AA6016 sheet following the experimental setup. The developed material model presented in the previous sections is employed in this simulation. Moreover, the Triboform built-in friction function in the software is adopted in this simulation to follow the industrial standards. The blank is modeled by

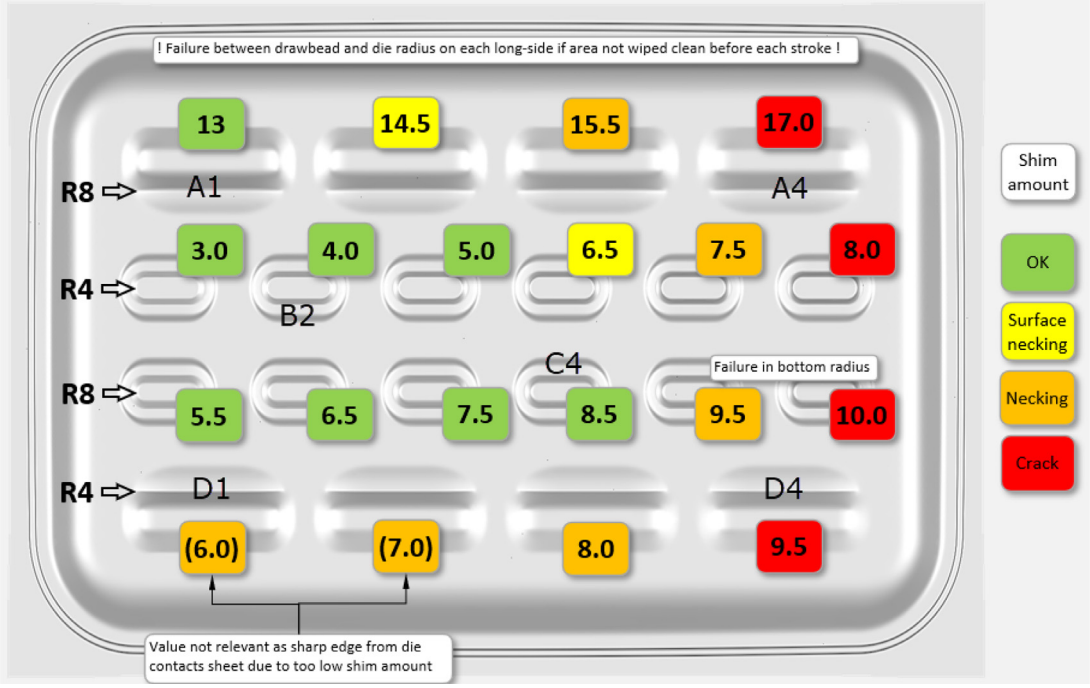

Fig. 14. An image of the stamped AA6016 panel with the VCBC test die.

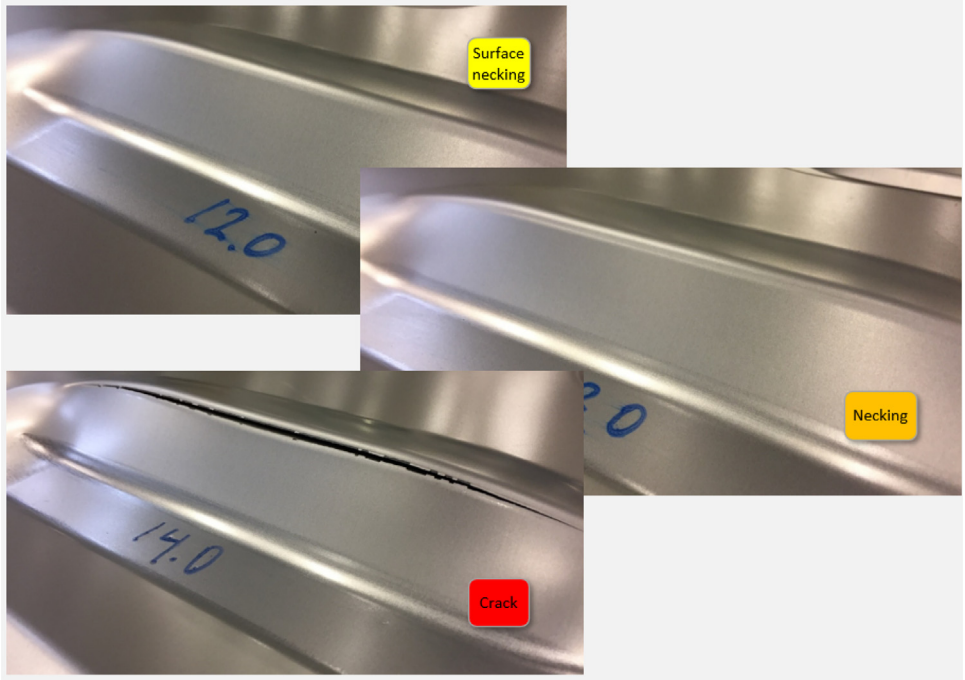

Fig. 15. An example of failure evaluation of aluminum alloy stamped panels conducted at VCBC.

the EPS-11 elements with an initial element size of 20 mm. The mesh-size refinement function in AutoForm is set up at level 5 to achieve the simulated results within a reasonable time. That creates the smallest element size of 0.625 mm.

For this simulated panel, a critical necking index should be lower than the necking indexes reported in Table 5 for several reasons. At first, the lubricated condition applied in the test die stamping is different from those of the lab-scale tests in both experimental and simulated manners. Secondly, the size of elements used in the test die simulation is significantly larger than that used in the simulations of stretch–bend tests due to the difference in the blank dimensions. Thirdly, the deformation of the critical regions of the test die panel is much

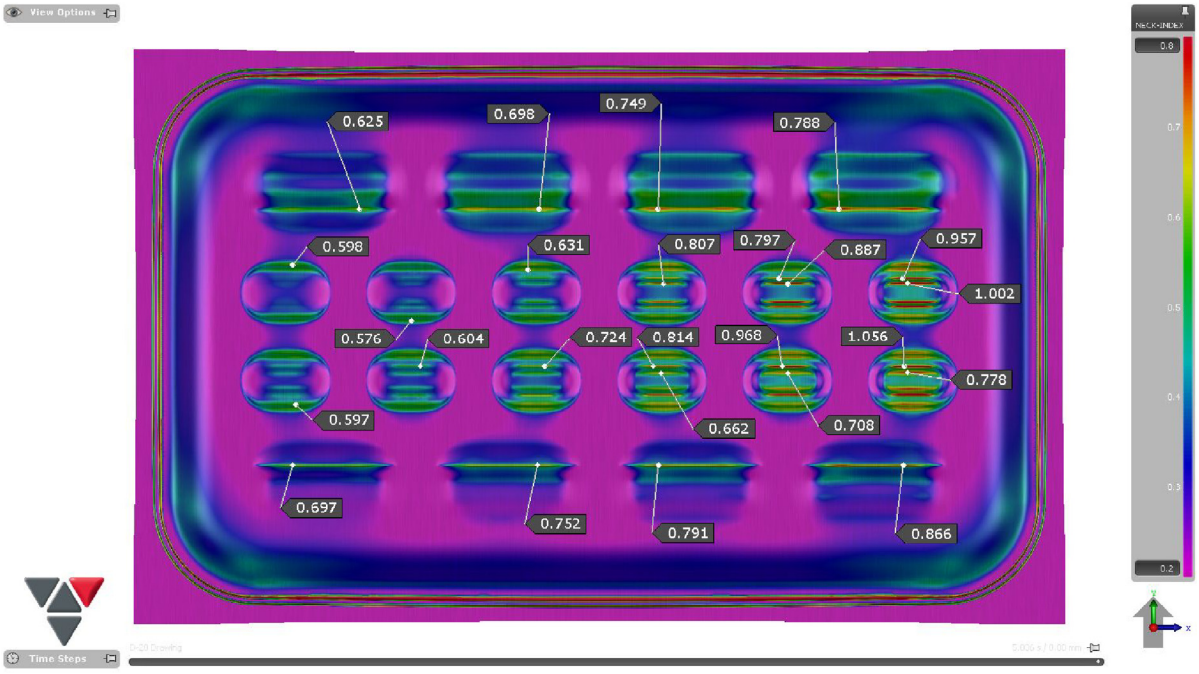

(a) Top view of the necking index distribution

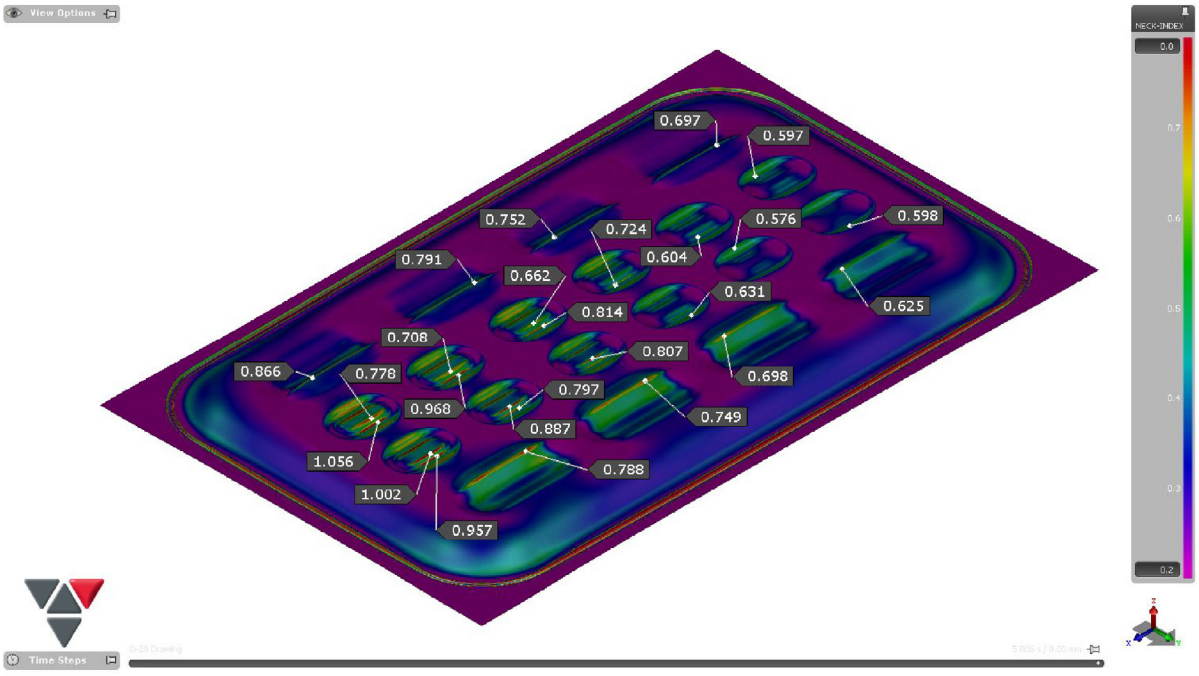

(b) Isometric view of the necking index distribution

Fig. 16. Simulated AA6016 panel subjected to the test die stamping procedure.

more complicated than that of the stretch–bend tests. For instance, the combined stretch–bending deformation is expected in the deformation of rows A and D of the panel; meanwhile, the bending and reverse bending modes are expected in regions B and C. Therefore, a trade-off value of the critical necking index should be used to balance the overestimation of the isotropic hardening law used in this simulation. Fig. 16 shows the calculated necking index distribution on the stamped panel, and Fig. 17 presents a closer view of the failure regions. In these figures, the upper limit of the color bar is set at 0.8 for visualizing the critical zones. Moreover, the numbers in these figures indicate the local maximums necking index of critical elements. For better visualization of these indexes, the reader is recommended to see the digital version of this article.

Generally, the proposed modeling approach presents good predictions for the necking and failure of the panel. Within each row, the necking index increases from the left to the right of the panel, which

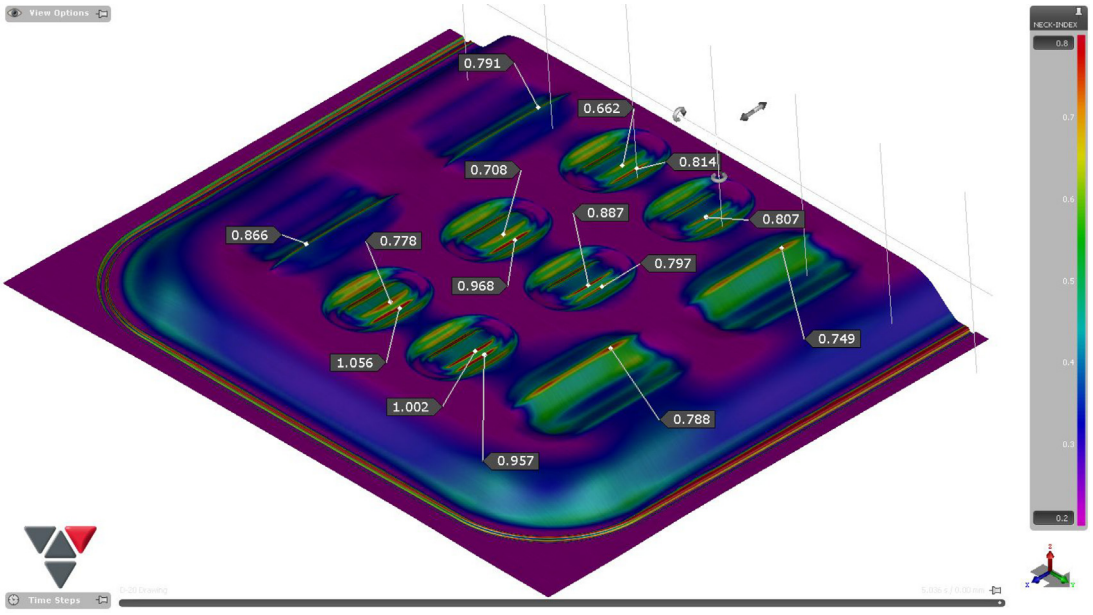

Fig. 17. A focused view of the simulated panel with the necking index distribution.

is agreed with the experimental observations of necking and crack positions, shown in Fig. 14.

Among the crack regions in the experiment, the minimum necking index is 0.788, observed in the A4 area, whereas the maximum is 1.056, observed in the C6 region. The predicting indexes for the surface necking and necking regions range from 0.697 to 0.968. The maximum index of the safe areas (except for the C3 and C4) is 0.625. Comparisons clarify that the difference between the safe and unsafe forms is marginal but can be indicated by setting the critical necking index of 0.65, for example. Furthermore, the simulation successfully predicted the failure locations of the challenging regions B5–B6 and C5–C6. In detail, the failure is expected to occur at the top surface of the B5–B6 areas and at the bottom surface of the C5–C6 parts, which is agreed well with the experimental observation. These failure locations were unable to be predicted in the previous study [54].

However, the simulation overestimated the failure status of two regions, B4 and C4, compared with the experimental evaluation. As discussed before, there are several issues related to the accuracy of the necking prediction for this panel stamping, which can be improved. For example, employing a kinematic hardening model may provide better predictions for the deformation of rows B and C since these areas underwent bending and reverse bending loads. Even with the mismatch, it is undeniable that the presented modeling approach provides an efficient way to predict the failure of sheet metal subjected to combined stretch–bending loads during the stamping procedure.

6. Discussion and conclusion

6.1. Discussion

In this study, four lab-scale stretch–bending tests with tool radii of 3, 6, 10, and 50 mm were conducted to calibrate the necking limits of DP800 and AA6016 sheets. The tool radii are selected to cover the range of common bending curvatures that occur in the stamping of automotive parts. Additional stretch–bending tests (e.g., the VDA 238-100 bending test) can be carried out to enrich the experimental data set used to identify the curves. In such a case, not only the reliability of the forming limits is increased but also the experimental cost rises.

The limit curve was constructed under the plane-strain forming mode. This concept can be easily extended to other forming modes by varying the parameter A_1 in Eq. (2) according to the strain increment ratio, $\beta = \Delta\varepsilon_2/\Delta\varepsilon_1$. One promising example of the extended necking limit application is the biaxial tension observed in the small punch tests [55,56].

The stretching-to-bending ratio ρ was formulated based on the strain gradient through the thickness direction of the element. In the numerical aspect, geometrical factors such as the element's size and the current thickness of the element may affect its computed strain components. The effect of those factors will be studied in future work.

Bending and reverse bending loads commonly occur in sequences during sheet metal stamping processes. Hence, employing a kinematic hardening model may provide better predictions for strain evolution than the isotropic hardening model used in this study. To reach this goal, additional tests, such as tension–compression–tension tests or shear-reverse-shear tests, should be conducted to calibrate the kinematic hardening parameters.

In practice, the accuracy of a simulation for strain localization with shell elements relies on many factors, including but not limited to the friction model, the element type, the mesh size, and the solver tolerance. The balance between the simulation accuracy and the affordable resources of time and equipment should be taken into account. For example, the simulation time of the stamping AA6016 panel described in the previous section is around one hour within the current configuration. Decreasing the smallest element size by 20% will increase the simulation time more than twelve times. Therefore, the use of the necking index ξ and the constant c_0 should be an alternative way to adapt the model in applications.

6.2. Conclusion

This study presents a modeling approach to predict strain localization while simulating sheet metal stamping processes with shell elements. In this approach, the limited strain is suggested to be a function of the stretching-to-bending ratio. The approach was applied to predict the failure of a stamped AA6016 panel to validate its application. The following conclusions can be made after this work:

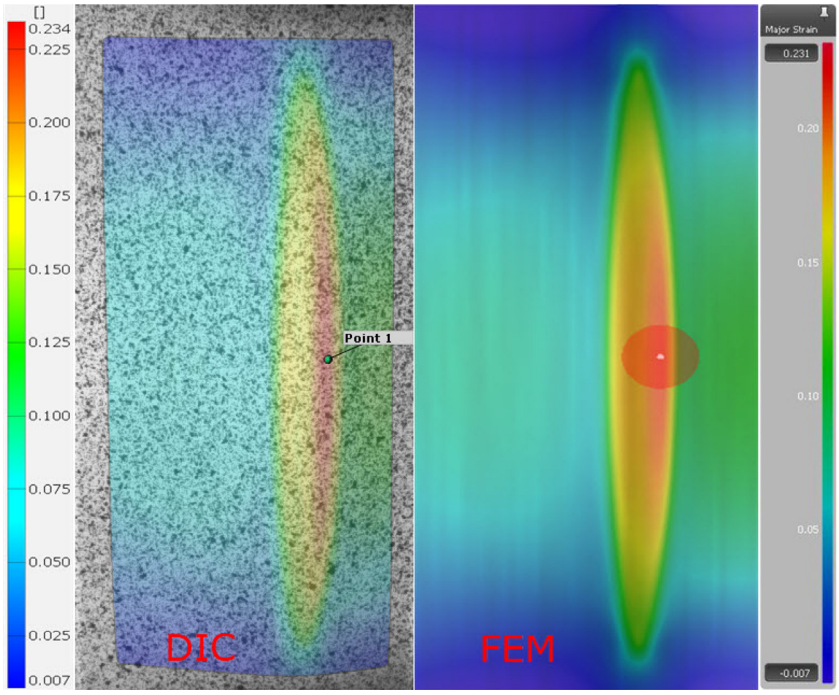

Fig. A.1. Comparison between measured and predicted strain distributions on the outer surface of the deformed AA6016 specimen observed at the necking stage of the R6 stretch–bend test.

1. The concept of stretch–bend necking limit was proposed based on the stretching-to-bending ratio. This ratio was formulated based on the through-thickness strain gradient of the considering element and classified the deformation in a range from pure stretching to pure bending. This phenomenon approach is adopted to explain the effect of combined stretch–bending loads on the failure of sheet metal.
2. Constitutive models calibrated with data obtained from uniaxial tensile and bulge tests provide excellent predictions for material behaviors of DP800 and AA6016 sheets subjected to stretch–bending tests. Based on experimental measurements and simulations of these tests, a hybrid experiment-simulation approach is adopted to identify the stretch–bend necking strain limits for the tested materials. Compared to the experimental data available in the literature, the calibrated necking limit curves present concordant predictions for the necking strains in the region of large stretching-to-bending ratios.
3. The identified necking limit curve of the AA6016 sheet is employed in AutoForm R10 software to simulate the stamping process with a test die developed at VCBC. The predicted results are promising, where the simulation correctly classified the safe and necking/crack status of 18 over 20 regions and overestimated the two remains. This verifies the potential of the proposed approach in predicting the failure of sheet metals subjected to industrial stamping processes.

CRediT authorship contribution statement

Quoc Tuan Pham: Writing – review & editing, Writing – original draft, Validation, Software, Resources, Methodology, Investigation, Formal analysis, Data curation, Conceptualization. **Md Shafiqul Islam:** Writing – review & editing, Writing – original draft, Funding acquisition, Formal analysis, Data curation, Project administration, Supervision. **Alexander Barlo:** Writing – review & editing, Writing – original draft, Software, Investigation, Formal analysis, Data curation, Validation. **Mats Sigvant:** Writing – review & editing, Writing – original draft, Visualization, Software, Investigation, Formal analysis, Conceptualization, Supervision. **Lluís Pérez Caro:** Writing – original draft, Validation, Resources, Investigation, Formal analysis, Data curation. **Kristoffer Trana:** Writing – original draft, Visualization, Validation, Resources, Formal analysis.

Declaration of competing interest

The authors declare the following financial interests/personal relationships which may be considered as potential competing interests: Md Shafiul Islam reports financial support was provided by Sweden's Innovation Agency. Md Shafiul Islam reports financial support was provided by KK-Stiftelsen.

Data availability

Data will be made available on request

Acknowledgments

The authors gratefully acknowledge the financial support from VINNOVA in the Sustainable Production subprogram within Vehicle Strategic Research and Innovation (FFI) program (grant number 2020-02986) and KK-Stiftelsen (grant number 20200125). Open Access funding was provided by the Blekinge Institute of Technology, Sweden.

Appendix

This Appendix presents the comparison between the strain distribution observed at the necking stage during the stretch–bending experiments of AA6016 sheet with their corresponding simulations. (See Figs. A.1–A.3.)

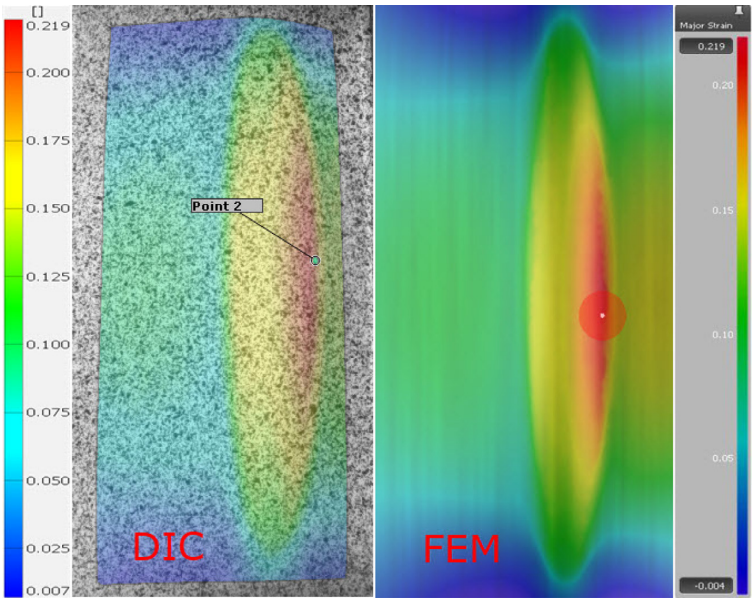

Fig. A.2. Comparison between measured and predicted strain distributions on the outer surface of the deformed AA6016 specimen observed at the necking stage of the R10 stretch–bend test.

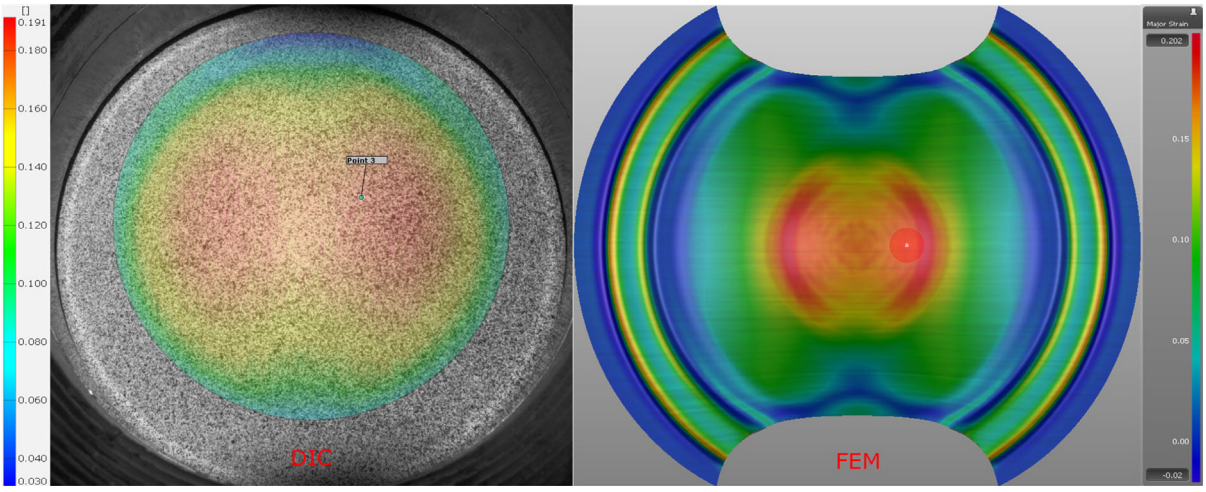

Fig. A.3. Comparison between measured and predicted strain distributions on the outer surface of the deformed AA6016 specimen observed at the necking stage of the Nakajima test.

References

[1] T.B. Stoughton, X. Zhu, Review of theoretical models of the strain-based FLD and their relevance to the stress-based FLD, Int. J. Plast. 20 (8–9) (2004) 1463–1486.
[2] W. Volk, J. Suh, Prediction of formability for non-linear deformation history using generalized forming limit concept (GFLC), in: AIP Conference Proceedings, volume 1567, (1) American Institute of Physics, 2013, pp. 556–561.
[3] T.B. Stoughton, J.W. Yoon, Path independent forming limits in strain and stress spaces, Int. J. Solids Struct. 49 (25) (2012) 3616–3625.
[4] W.Y. Chien, J. Pan, S.C. Tang, A combined necking and shear localization analysis for aluminum sheets under biaxial stretching conditions, Int. J. Plast. 20 (11) (2004) 1953–1981.
[5] M. Kuroda, V. Tvergaard, Effects of texture on shear band formation in plane strain tension/compression and bending, Int. J. Plast. 23 (2) (2007) 244–272.
[6] D. Kitting, M. Koplenig, A. Ofenheimer, H. Pauli, E.T. Till, Application of a "concave-side rule" approach for assessing formability of stretch-bent steel sheets, Int. J. Mater. Form. 2 (1) (2009) 427–430.
[7] V. Grolleau, C.C. Roth, V. Lafilé, B. Galpin, D. Mohr, Loading of mini-nakazima specimens with a dihedral punch: Determining the strain to fracture for plane strain tension through stretch-bending, Int. J. Mech. Sci. 152 (2019) 329–345.
[8] J. Noder, A. Abedini, C. Butcher, Evaluation of the VDA 238–100 tight radius bend test for plane strain fracture characterization of automotive sheet metals, Exp. Mech. 60 (6) (2020) 787–800.
[9] R.G. Andersen, J.G. Londono, P.B. Woelke, K.L. Nielsen, Fundamental differences between plane strain bending and far-field plane strain tension in ductile plate failure, J. Mech. Phys. Solids 141 (2020) 103960.
[10] J.H. Kim, J.H. Sung, K. Piao, R.H. Wagoner, The shear fracture of dual-phase steel, Int. J. Plast. 27 (10) (2011) 1658–1676.
[11] M. Luo, T. Wierzbicki, Numerical failure analysis of a stretch-bending test on dual-phase steel sheets using a phenomenological fracture model, Int. J. Solids Struct. 47 (22–23) (2010) 3084–3102.
[12] Z.C. Xia, D. Zeng, Sheet metal forming limit under stretch-bending, in: International Manufacturing Science and Engineering Conference, Vol. 48517, 2008, pp. 661–667.
[13] J.-w. Lee, F. Barlat, Analytical approach to failure determination of advanced high-strength steel in stretch-bending mode, Steel Res. Int. 92 (1) (2021) 2000124.
[14] M.R. Tharrett, T.B. Stoughton, Stretch-Bend Forming Limits of 1008 AK Steel, Technical Report, SAE Technical Paper, 2003.
[15] T.B. Stoughton, J.W. Yoon, A new approach for failure criterion for sheet metals, Int. J. Plast. 27 (3) (2011) 440–459.
[16] D. Morales-Palma, C. Vallellano, F.J. García-Lomas, Assessment of the effect of the through-thickness strain/stress gradient on the formability of stretch-bend metal sheets, Mater. Des. 50 (2013) 798–809.
[17] C. Vallellano, D. Morales, A. Martinez, F. García-Lomas, On the use of concave-side rule and critical-distance methods to predict the influence of bending on sheet-metal formability, Int. J. Mater. Form. 3 (1) (2010) 1167–1170.

[18] S. Sriram, C. Wong, M. Huang, B. Yan, Stretch bendability of advanced high strength steels, SAE Trans. (2003) 641–649.
[19] J. Wu, D. Zhou, L. Zhang, Y. Zhou, C.Q. Du, M.F. Shi, A failure criterion for stretch bendability of advanced high-strength steels, SAE Trans. (2006) 311–319.
[20] F.M. Neuhauser, O. Terrazas, N. Manopulo, P. Hora, C. Van Tyne, The bending dependency of forming limit diagrams, Int. J. Mater. Form. 12 (5) (2019) 815–825.
[21] M. Kõrgesaar, H. Remes, J. Romanoff, Size dependent response of large shell elements under in-plane tensile loading, Int. J. Solids Struct. 51 (21–22) (2014) 3752–3761.
[22] A.E. Tekkaya, State-of-the-art of simulation of sheet metal forming, J. Mater Process. Technol. 103 (1) (2000) 14–22.
[23] K. Pack, D. Mohr, Combined necking & fracture model to predict ductile failure with shell finite elements, Eng. Fract. Mech. 182 (2017) 32–51.
[24] M. Dunand, D. Mohr, Hybrid experimental–numerical analysis of basic ductile fracture experiments for sheet metals, Int. J. Solids Struct. 47 (9) (2010) 1130–1143.
[25] K. Pack, T. Tancogne-Dejean, M.B. Gorji, D. Mohr, Hosford-Coulomb ductile failure model for shell elements: Experimental identification and validation for DP980 steel and aluminum 6016-T4, Int. J. Solids Struct. 151 (2018) 214–232.
[26] L. Wei, F. Qin, K. Cui, Prediction the stainless steel sheet fracture with mesh size effect for shell elements, Int. J. Solids Struct. 210 (2021) 35–48.
[27] F. Neukamm, M. Feucht, A. Haufe, K. Roll, On closing the constitutive gap between forming and crash simulation, in: 10th International LS-DYNA Users Conference, 2008, pp. 12–21.
[28] F. Neukamm, M. Feucht, A. Haufe, Considering damage history in crashworthiness simulations, 2009, Ls-Dyna Anwenderforum.
[29] M. Basaran, S.D. Wölkerling, M. Feucht, F. Neukamm, D. Weichert, S. DAIMLER AG, An extension of the GISSMO damage model based on lode angle dependence, 15, 2010, p. 15, LS-DYNA Anwenderforum.
[30] F.X.C. Andrade, M. Feucht, A. Haufe, F. Neukamm, An incremental stress state dependent damage model for ductile failure prediction, Int. J. Fract. 200 (1) (2016) 127–150.
[31] T. Borrvall, T. Johansson, M. Schill, J. Jergeus, K. Mattiasson, P. DuBois, A general damage initiation and evolution model in LS-DYNA, in: 9th European LS-DYNA Conference, Manchester, UK, 2013.
[32] Z. Marciniak, K. Kuczyński, Limit strains in the processes of stretch-forming sheet metal, Int. J. Mech. Sci. 9 (9) (1967) 609–620.
[33] P.B. Woelke, Simplification of the gurson model for large-scale plane stress problems, Int. J. Plast. 125 (2020) 331–347.
[34] V. Tvergaard, On localization in ductile materials containing spherical voids, Int. J. Fract. 18 (4) (1982) 237–252.
[35] J. Min, T.B. Stoughton, J.E. Carsley, J. Lin, Compensation for process-dependent effects in the determination of localized necking limits, Int. J. Mech. Sci. 117 (2016) 115–134.
[36] L. Zhang, J. Min, J.E. Carsley, T.B. Stoughton, J. Lin, Experimental and theoretical investigation on the role of friction in nakazima testing, Int. J. Mech. Sci. 133 (2017) 217–226.
[37] K. Chung, H. Kim, C. Lee, Forming limit criterion for ductile anisotropic sheets as a material property and its deformation path insensitivity. Part I: Deformation path insensitive formula based on theoretical models, Int. J. Plast. 58 (2014) 3–34.
[38] M. Costas, D. Morin, O.S. Hopperstad, T. Børvik, M. Langseth, A through-thickness damage regularisation scheme for shell elements subjected to severe bending and membrane deformations, J. Mech. Phys. Solids 123 (2019) 190–206.
[39] M.G. Cockcroft, Ductility and workability of metals, J. Met. 96 (1968) 2444.
[40] ISO 7438:2016 (E), Metallic Materials–Bend Test, Technical Report, International Organization for Standardization, Geneva, CH, 2016.
[41] M. Gorji, B. Berisha, P. Hora, F. Barlat, Modeling of localization and fracture phenomena in strain and stress space for sheet metal forming, Int. J. Mater. Form. 9 (5) (2016) 573–584.
[42] T. Beerli, V. Grolleau, D. Mohr, C.C. Roth, Axisymmetric V-bending: A single experiment to determine the fracture strain and weakest sheet material direction for plane strain tension, Int. J. Solids Struct. 252 (2022) 111813.
[43] Q.-T. Pham, B.-H. Lee, K.-C. Park, Y.-S. Kim, Influence of the post-necking prediction of hardening law on the theoretical forming limit curve of aluminium sheets, Int. J. Mech. Sci. 140 (2018) 521–536.
[44] M. Sigvant, K. Mattiasson, H. Vegter, P. Thilderkvist, A viscous pressure bulge test for the determination of a plastic hardening curve and equibiaxial material data, Int. J. Mater. Form. 2 (4) (2009) 235–242.
[45] H. Swift, Plastic instability under plane stress, J. Mech. Phys. Solids 1 (1) (1952) 1–18.
[46] J.E. Hockett, O.D. Sherby, Large strain deformation of polycrystalline metals at low homologous temperatures, J. Mech. Phys. Solids 23 (2) (1975) 87–98.
[47] D. Banabic, Sheet Metal Forming Processes: Constitutive Modelling and Numerical Simulation, Springer Science & Business Media, 2010.
[48] AutoForm Engineering GmbH, AutoForm forming R10 manual: Elasto-plastic shell element, 2023, https://servicecenter.autoform.com/smf10/en/autoform-formingsolver/elements/elasto-plastic-shell-element. (Online; Accessed 11 April 2023).
[49] A. Barlo, N. Manopulo, M. Sigvant, B. Endelt, K. Trana, Investigation OF a BENDING CORRECTED FORMING LIMIT SURFACE FOR failure prediction IN SHEET METALS, in: Forming Technology Forum, 2019.
[50] M. Sigvant, K. Mattiasson, M. Larsson, The definition of incipient necking and its impact on experimentally or theoretically determined forming limit curves, in: Proceedings of IDDRG'08, the International Deep Drawing Research Group, June 16-18, Olofström, Sweden, Edited By Nader Asnafi, 2008.
[51] J.-y. Kim, B. Hance, The combined influence of global and local formability on the vda 238-100 bending angle in advanced high-strength steels, in: International Automotive Body Congress, Global Automotive Management Council, 2022.
[52] L. Mattei, D. Daniel, G. Guiglionda, H. Klöcker, J. Driver, Strain localization and damage mechanisms during bending of AA6016 sheet, Mater. Sci. Eng. A 559 (2013) 812–821.
[53] VDA 238-100, Test specification: plate bending test for metallic materials, (2017).
[54] A.B.K. Barlo, Investigation of Alternative Evaluation Spaces for Failure Prediction in Sheet Metals, Aalborg University, 2019.
[55] S. Arunkumar, Overview of small punch test, Met. Mater. Int. 26 (6) (2020) 719–738.
[56] J. Torres, A.P. Gordon, Mechanics of the small punch test: A review and qualification of additive manufacturing materials, J. Mater. Sci. 56 (18) (2021) 10707–10744.